

Combo Loss: Handling Input and Output Imbalance in Multi-Organ Segmentation

Saeid Asgari Taghanaki^{1,2}, Yefeng Zheng², *Senior Member, IEEE*, S. Kevin Zhou², *Senior Member, IEEE*,
Bogdan Georgescu², *Senior Member, IEEE*, Puneet Sharma², Daguang Xu²,
Dorin Comaniciu², *Fellow, IEEE*, and Ghassan Hamarneh¹, *Senior Member, IEEE*

¹Medical Image Analysis Lab, School of Computing Science, Simon Fraser University, Canada

²Medical Imaging Technologies, Siemens Healthineers, Princeton, NJ, USA

Simultaneous segmentation of multiple organs from different medical imaging modalities is a crucial task as it can be utilized for computer-aided diagnosis, computer-assisted surgery, and therapy planning. Thanks to the recent advances in deep learning, several deep neural networks for medical image segmentation have been introduced successfully for this purpose. In this paper, we focus on learning a deep multi-organ segmentation network that labels voxels. In particular, we examine the critical choice of a loss function in order to handle the notorious imbalance problem that plagues both the input and output of a learning model. The input imbalance refers to the class-imbalance in the input training samples (i.e. small foreground objects embedded in an abundance of background voxels, as well as organs of varying sizes). The output imbalance refers to the imbalance between the false positives and false negatives of the inference model. We introduce a loss function that integrates a weighted cross-entropy with a Dice similarity coefficient to tackle both types of imbalance during training and inference. We evaluated the proposed loss function on three datasets of whole body PET scans with 5 target organs, MRI prostate scans, and ultrasound echocardiography images with a single target organ. We show that a simple network architecture with the proposed integrative loss function can outperform state-of-the-art methods and results of the competing methods can be improved when our proposed loss is used.

Index Terms—Class-imbalance, output-imbalance, deep convolutional neural networks, loss function, multi-organ segmentation

I. INTRODUCTION

ORGAN segmentation is an important processing step in medical image analysis, e.g. for image guided interventions, radiotherapy, or improved radiological diagnostics. A plethora of single/multi-organ segmentation methods including machine/deep learning approaches has been introduced in the literature for different medical imaging modalities, e.g. magnetic resonance imaging, and positron emission tomography (PET). We summarize the recent machine/deep learning-based organ segmentation works in Table I.

Organ segmentation methods can be categorized into two main groups: machine learning and non-machine learning based methods. Among the non-machine learning approaches, aside from image-processing based methods (e.g. thresholding, watershed, morphological operations), optimization based methods have been most popular in the past few decades. Optimization based methods can be further divided into optimization based segmentation and registration. In optimization based segmentation, a (single or multi-region) shape representation, such as parameterized surfaces, level-sets, and label fields, are initialized and optimized to minimize a target energy functional with data and regularization terms [20]–[24]. Leveraging voxel based image registration for segmentation has also been popular, in which a pre-segmented image or images (i.e. single or multi-atlas) are registered to novel images, by optimizing a spatial transformation (e.g. rigid or non-rigid) to maximize an image-to-image similarity metric [25]–[28]. However, these methods require heavy computation, parameter settings and

user interaction. Furthermore, they are normally very slow, sometimes, taking hours to process one volume.

Among machine (statistical) learning based methods, random decision forests [2], [7] obtained more attention compared to other methods e.g. support vector machines [6], however, they require large number of hand-crafted features. Thus, as training is not end-to-end, there is no learned relation between the extracted features and classifier. This missing connection results in redundant and/or non-discriminatory feature extraction.

More recently, deep learning based medical image segmentation approaches have gained great popularity [29]–[34]. Several deep convolutional segmentation models in the form of encoder-decoder networks have been proposed for both medical and non-medical images e.g. 2D U-Net [35], 3D U-Net [36], 3D V-Net [37], 2D SegNet [38] to learn features and classify/segment images simultaneously in an end-to-end manner. These models with/without modifications have been widely applied to both binary and multiclass medical image segmentation problems. Specifically, for organ segmentation, Cha et al. [39] applied a patch based CNN method to label each center pixel in a patch to segment bladder from CT scans. However, using only local patches to label center pixels is prone to both false negative (i.e. failure to segment multiple organs with similar intensities/appearances) and false positive errors (small island-like erroneous segmented regions). Also, the densely extracted patches increase the computational cost and running time. Hu et al. [13] proposed a convolutional neural network (CNN) based method to segment multiple organs from CT scans. They applied an energy based refining step to improve the CNN segmentation results. Similarly, Gibson et al. [18] applied a threshold based refining step to

TABLE I: Organ localization and/or segmentation works. In the Table, BR, HR, RK, LK, BL, LV, ST, PN, and SP stand for brain, heart, right kidney, left kidney, bladder, liver, stomach, pancreas, and spleen. Algn., MisO., Lcl., Sg., and Trsh. mean whether the methods require all the images to be aligned, handle missing organs, perform organ localization and/or segmentation, are based on thresholding.

Work	Year	Method	Modality	Organs									Algn.	MisO.	Lcl.	Sg.	Trsh.	2D/3D	(train, test)
				BR	HR	RK	LK	BL	LV	ST	PN	SP							
Zheng et al. [1]	2008	MSL	CT & MRI		✓					✓					✓	✓	2D/3D	(400, 395) (226, 3F)	
Criminisi et al. [2]	2009	RF	CT		✓	✓	✓					✓			✓		3D	(19, 19)	
Criminisi et al. [3]	2010	RF	CT		✓	✓	✓	✓							✓		3D	(55, 45)	
Criminisi et al. [4]	2013	RegF	CT		✓	✓	✓					✓			✓	✓	3D	(318, 82)	
Fischer et al. [5]	2014	RF	PET	✓		✓	✓	✓									3D	(20, 5)	
Bi et al. [6]	2014	SVM	PET+CT	✓	✓	✓	✓	✓				✓		✓	✓	✓	2D	(33, LOO)	
Gauriau et al. [7]	2015	RegF	CT			✓	✓					✓		✓	✓	✓	3D	(50, 58)	
Bi et al. [8]	2015	FS+SVM	PET+CT	✓	✓	✓	✓	✓				✓		✓	✓	✓	2D	(20, 20)	
Bruke et al. [9]	2015	Atlas GMM	CT			✓	✓					✓		✓	✓		3D	(40, 60)	
Marsousi et al. [10]	2015	Atlas	US			✓						✓		✓	✓		3D	(6, 30)	
Bi et al. [11]	2016	S.pixel+SVM	PET+CT	✓	✓	✓	✓	✓				✓		✓	✓	✓	2D	(20, 20)	
Ahmadvand et al. [12]	2016	RF	PET	✓	✓	✓	✓					✓		✓	✓		3D	(10, 15)	
Hu et al. [13]	2017	CNN	CT			✓	✓		✓								3D	(120, 20)	
Samarakoon et al. [14]	2017	LRegF	CT			✓	✓					✓		✓			3D	(55, 45)	
Richberg et al. [15]	2017	CNN	US			✓	✓					✓		✓			3D	(126, 42)	
Vos et al. [16]	2017	Conv-net	CT		✓									✓			2D	(144, 67) (81, 19)	
Yang et al. [17]	2017	GAN+CNN	CT					✓							✓		3D	(1063, 50)	
Gibson et al. [18]	2017	Dilated CNN	CT					✓	✓	✓							3D	(72, 8F)	
Bobo et al. [19]	2018	CNN	MRI			✓	✓	✓	✓		✓		✓	✓			3D	(35, 10)(111, 27)	
Proposed	2018	Deep model	PET & MR & US	✓	✓	✓	✓	✓				✓		✓	✓		3D	(40, 18) (700, 258) (430, 20)	

cope with false positives produced by their CNN based organ segmentation model. Yang et al. [17] proposed an adversarial based image-to-image network to segment liver from CT scans. They also applied a post processing step to reduce both false positives and false negatives.

A key step to train such deep networks is to properly formulate a loss function. U-Net (both 2D and 3D) and 2D SegNet minimize cross entropy loss to mimic ground truth segmentation masks for an input image while 3D V-Net applies the Dice based loss function.

When performing segmentation especially using deep networks, one has to cope with two types of imbalance issues:

a) Input imbalance or inter-class-imbalance during training, i.e. much fewer foreground pixels/voxels relative to the large number of background voxels in binary segmentation, and smaller objects/classes in a multi-class segmentation relative to other larger objects/classes and the background. Therefore, classes with more observations (i.e. voxels) overshadow the minority classes.

b) Output imbalance. During inference, it is unavoidable to have false positives and false negatives. False positives are the background voxels (or other objects in case of multi-class) that are wrongly labeled as the target object. False negatives refer to the voxels of a target object that are erroneously labeled as background or, in the case of multi-organ segmentation, are labelled as some other organs. Clearly, eliminating both false positives and false negatives is the ultimate ideal. However, in practical systems, one increases as the other decreases. For certain applications, reducing the false positive rate is more important than reducing the false negative rate or vice versa. The following are example cases where FP should be penalized more: to handle missing organs, to prevent a model from segmenting normal active regions in PET image segmentation i.e. relatively high intensity regions compared to background which are considered as neither lesion nor

organ, to prevent small island-like segmented regions from another organs or background in multi-organ segmentation, false positives should be penalized more. In contrast, for some other applications false negatives should be penalized more, e.g. in ultrasound image segmentation where the boundaries of organs are not very clear, usually under-segmentation happens or in MRI segmentation some wholes (small not). However, conventional cost functions lack a systematic way of controlling the trade-off between false positive and false negative rates.

Cross entropy is commonly used as a loss function in deep learning. Although it can potentially control output imbalance i.e. false positives and false negatives, it has sub-optimal performance when segmenting highly input class-imbalanced images [38]. There are several ways of handling input imbalance in general classification tasks, e.g. random over/under sampling, SMOTE [40]. However these methods and similar approaches are not directly applicable or meaningful to segmentation problems as it requires producing more or removing some pixels/voxels to balance the different classes within each image. Therefore, several different techniques such as weighted cross entropy [41], median frequency balancing as used in 2D SegNet [38], the Dice optimization function as used in the 3D V-Net method [37], and a focal loss function [42] have been proposed.

Among all methods introduced for tackling the input-imbalance problem, the Dice based loss function has shown better performance for binary-class segmentation problems [41]. However, the ability of the Dice loss function to control the trade-off between false positives and false negatives i.e. output imbalance has not been explored in previous works. Controlling the trade-off is not a trivial issue for some medical images and it is not easy to be controlled with classical Dice optimization function. In this paper, we leverage both the cross entropy (pixel based) and the Dice optimization (shape based)

functions to define a new loss function that handles both of the aforementioned input and output imbalance types.

In this paper, we make the following contributions: a) We introduce a new multi-loss function to handle input and output imbalance in segmentation problems. b) Our proposed loss improves previous deep models namely 3D U-Net, 3D V-Net, and our extended version of 2D SegNet i.e. 3D SegNet both in training and testing for single and multi-organ segmentation from different modalities. c) The proposed loss function, by controlling the trade-off between false positives and negatives, is able to handle missing organs i.e. by penalizing more the false positives. d) We extend 3D U-Net and 3D V-Net from binary to multiclass segmentation models. e) We introduce the first volumetric (and first deep) multi-organ semantic model which simultaneously segments and classifies multiple organs from whole body 3D PET scans. PET organ segmentation is useful when a corresponding CT image is not available to help with detecting organs. Even if a corresponding CT image is available, usually PET and CT need to be registered.

II. METHOD

Given a medical image volume, the goal is to predict the class of each voxel by assigning an activation value $p(x) \in [0, 1]$ to each voxel x . We adopt a deep learning technique to learn a prediction model $\Phi(x; \theta) : x \rightarrow p(x)$, where θ denotes the model parameters and p_i is activation value for organ/class i .

Cross Entropy Loss Function. For multi-class problems, the cross entropy loss can be computed as $C = \sum_x \sum_i t_i \ln(p_i)$ where p is the predicted probability mass function (PMF), i.e. assigning a probability/activation value to each class for each voxel, and t is the one-hot encoded target (or ground truth) PMF, where the index i iterates over the number of organs and x over the number of the samples (i.e. voxels). C can be computed as a sum of several binary cross entropy terms, which for some multi-class problems, as in this paper, makes it possible to have control over false positives/negatives. In the case of binary classification, C can be rewritten as $\sum_x t_1 \ln(p_1) + (1 - t_1) \ln(1 - p_1)$. The term $(1 - t_1) \ln(1 - p_1)$ penalizes false positives as it is zero when the prediction is correct. The binary formulation can also be extended and used for multi-class problems as $\frac{1}{N} \sum_{i=1}^N t_i \ln(p_i) + (1 - t_i) \ln(1 - p_i)$ where $N = \text{number of classes} \times \text{number of samples}$. Therefore, output is average of multiple binary cross entropies.

Dice Optimization Function. The Dice function is a widely used metric for evaluating image segmentation accuracy, which can be written in forms of $Dice = \text{True positives} / (\text{number of positives} + \text{number of false positives})$ or $Dice = 2 \times TP / (FN + (2 \times TP) + FP)$. It can also be rewritten as a weighted function to generalize into multi-class problems [41]. However, when it is used as an optimization/loss function, it is not possible to control the penalization of either FPs or FN's separately or their trade-off in the above formulations.

Combo Loss. To leverage the Dice function that handles the input class-imbalance problem, i.e. segmenting a small

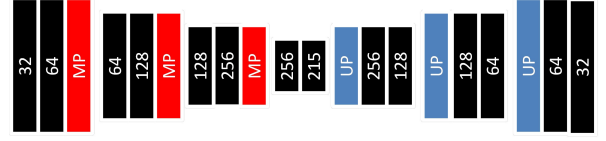


Fig. 1: The applied network architecture. Black: convolution $3 \times 3 \times 3$, MP: max-pooling $2 \times 2 \times 2$, UP: up-sampling $2 \times 2 \times 2$. The values inside the boxes show number of channels.

foreground from a large context/background, while at the same time controlling the trade-off between FP and FN using cross entropy, we introduce our loss L as a weighted sum of two terms: A Dice loss and a modified cross entropy, and is written as:

$$L = \alpha \sum_{i=1}^K \left(\frac{2 \sum_{i=1}^N p_i t_i}{\sum_{i=1}^N p_i + \sum_{i=1}^N t_i} \right) + (1 - \alpha) \times \left(\frac{1}{N} \sum_{i=1}^N \beta (t_i - \ln p_i) + (1 - \beta) [(1 - t_i) \ln(1 - p_i)] \right) \quad (1)$$

where α controls the amount of Dice term contribution in the loss function L , and $\beta \in [0, 1]$ controls the level of model penalization for false positives/negatives: when β is set to a value smaller than 0.5, FP are penalized more than FN as the term $(1 - t_1) \ln(1 - p_1)$ is weighted more heavily, and vice versa.

Model Parameter Optimization. To optimize the model parameters θ to minimize the loss, we use error back propagation, which relies on the chain rule. We calculate the gradient of L with respect to p_j , i.e. dL/dp_j ,

$$\frac{\partial L}{\partial p_j} = 2\alpha \sum_{i=1}^N \frac{t_i \left(\sum_{i=1}^N p_i + \sum_{i=1}^N t_i \right) - p_j \left(\sum_{i=1}^N p_i t_i \right)}{\left(\sum_{i=1}^N p_i + \sum_{i=1}^N t_i \right)^2} + (1 - \alpha) \times \left(\frac{1}{N} \sum_{i=1}^N \beta \left(\frac{t_i}{p_i} \right) + (1 - \beta) \left(-\frac{1 - t_i}{1 - p_i} \right) \right). \quad (2)$$

Then we calculate how the changes in the model parameters in the last layer of the deep architecture affect the predicted p_j , and so on.

Deep Model Architecture. We use the deep architecture shown in Fig. 1. This architecture departs from existing architectures like 3D U-Net, 3D U-Net, and 2D SegNet as listed in Table II. We adopt this simple network to show that the improvement in results is not attributed to some elaborate architecture and to validate our hypothesis that, even with a simple shallower architecture as long as a proper loss function is used, it is possible outperform more complex architectures e.g. networks with skip connections [35]–[37] or specific up-sampling [38].

Training. For multi-organ segmentation from whole body PET images, as the volumes are large to fit into memory, we extract random sub-volumes from each whole body scan

TABLE II: Comparison between our proposed method and state of the art deep learning segmentation methods

Network	Skipped connections	Loss	Upsampling	Parameters
2D SegNet [38]	No	Cross entropy	Specific (using pooling indices)	16,375,169
3D U-Net [36]	Yes	Cross entropy	Regular	12,226,243
3D V-Net [37]	Yes	Dice	Regular	84,938,241
Proposed	No	Proposed	Regular	13,997,827

to train a model. Each sub-volume could include voxels belonging to $n \in \{0, 1, \dots, K\}$ organs, with $n = 0$ indicating a sub-volume including only background. However, for binary segmentation i.e. 3D ultrasound and MRI datasets, we train using the entire volumes. On test data (only for PET), we apply a volumetric sliding window (with stride), i.e., a volumetric field of view V is partitioned into smaller sub-volumes $\{v_1, v_2, \dots, v_n\}$, where the size of v_i is the same as that of the training sub-volumes. Along any of the dimensions, the stride would be at least 1 voxel and at most the size of the sub-volume in that dimension. Larger strides speed up the computation at the expense of coarser spatial predictions. Let v_i be a subvolume with activation a_{v_i} , V_x be the set of subvolumes that include x , A_{V_x} be the set of corresponding activation values. $T(A_{V_x})$ is the set of indicator variables whose value is 1 if the activation is larger than t , and 0 otherwise, where t is a threshold value. Then, the label assigned to voxel x is given by: $f(x) = \begin{cases} 0, & \text{if } \max(T(A_{V_x})) = 0 \\ 1, & \text{otherwise} \end{cases}$. In other words, a single voxel x may reside within multiple overlapping subvolumes; if the activation of any these subvolumes is larger than threshold T , then x is assigned 1, and 0 otherwise.

III. IMPLEMENTATION DETAILS

a) PET multi-organ segmentation: For training the PET multi-organ segmentation network, from each training image, we extract 100 randomly positioned $80 \times 80 \times 80$ -voxel sub-volumes per organ (5 organs in total: brain, heart, left kidney, right kidney, and bladder) and another 100 for negative background sub-volumes. Therefore, we train all the models with $\sim 600 \times \text{no. training volumes}$. In test, the striding size was set to $20 \times 20 \times 20$. We train and test all the models using a Titan-X GPU with batch-size 1.

b) Ultrasound echocardiography and prostate MRI segmentation: We train and test all the models on these datasets with whole-volume images (i.e. not sub-volumes) using two M5000 GPUs with batch-size 2.

For all datasets, we initialize our models using Glorot_uniform [43] and train them with ADADELTA [44], with learning rate of 1, $\rho = 0.95$, $\epsilon = 1e - 08$, and $decay = 0$. All the models are coded using TensorFlow. To prevent gradient vanishing/exploding we use batch normalization after each convolution layer. It also allows us to use higher learning rate. We practically set the α and β in the proposed loss function. We found that the equal contribution (i.e. $\alpha = 0.5$) of pixel based and shape based terms gives the best results. However, we found that for the PET data, models need to be penalized more for false positives (i.e. $\beta = 0.4$) and for MRI and ultrasound data models need to be penalized more for false negatives (i.e. $\beta = 0.9$).

IV. DATASETS

For evaluation, we use three different datasets: a) 58 whole body PET scans of resolution $\sim 0.35 \times \sim 0.35 \times \sim 3.5 - 5$ mm. We randomly pick 10 whole body volumes for testing and train with the 48 remaining volumes. We normalize the intensity range of our training and testing volumes using the min-max method based on min and max intensity values of the whole training set. Next, in both training and testing, each single sub-volume is also normalized to $[0, 1]$ using its min and max before feeding it into network. b) 958 MRI prostate scans of different resolution which were resampled to voxel size of $1 \times 1 \times 3$ (mm). We randomly picked 258 volumes for testing, and train with remaining 700 volumes. c) Ultrasound echocardiography images of resolution $2 \times 2 \times 2$ (mm), used for left ventricular myocardial segmentation, were split into 430 train and 20 test. The datasets were collected internally and from The Cancer Imaging Archive (TCIA) QIN-HEADNECK and ProstateX datasets [45]–[49]. Samples of the three datasets are shown in Fig. 2.

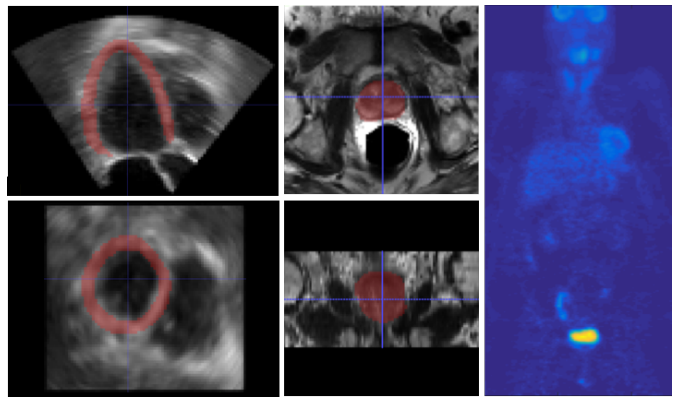


Fig. 2: Samples of the used datasets. The first column shows the left ventricular myocardium (highlighted in red) in ultrasound echocardiography. In the second column, the prostate is highlighted in red in an MRI scan. For MRI and ultrasound samples, the 2 rows show the axial and coronal views. Column 3 shows coronal view of a whole body PET scan.

V. RESULTS

Our evaluation is divided into 2 parts. First, in subsection V-A, we compare, both qualitatively and quantitatively, the performance of all the competing methods to the proposed method on the test data, for multi-organ segmentation from PET scans. We test different modification/variants of the proposed loss with the proposed architecture, i.e. cross entropy optimization (P_{CE}), weighted cross entropy (P_{WCE}), Dice optimization (P_D), Dice + cross entropy optimization (P_{DCE}), and the proposed loss (P_{Combo}).

TABLE III: Comparing the performance of competing methods with/without the proposed loss function vs. the proposed method for PET multi-organ segmentation

	Methods	Jaccard	Dice	FPR	FNR
a	3D U-Net [36]	0.55 ± 0.16	0.69 ± 0.16	0.41 ± 0.31	0.30 ± 0.15
	3D U-Net_Combo	0.68 ± 0.18	0.79 ± 0.15	0.18 ± 0.09	0.21 ± 0.17
b	3D V-Net [37]	0.52 ± 0.17	0.67 ± 0.16	0.89 ± 0.90	0.13 ± 0.09
	3D V-Net_Combo	0.55 ± 0.17	0.70 ± 0.15	0.64 ± 0.46	0.16 ± 0.11
c	3D SegNet	0.41 ± 0.20	0.56 ± 0.21	0.66 ± 0.78	0.32 ± 0.28
	3D SegNet_Combo	0.55 ± 0.19	0.69 ± 0.17	0.37 ± 0.38	0.28 ± 0.17
d	Ahmadvand et al. [12]	0.41 ± 0.18	0.53 ± 0.23	0.35 ± 0.77	0.37 ± 0.82
	P _C E	0.34 ± 0.15	0.49 ± 0.18	0.67 ± 0.42	0.48 ± 0.14
e	P _W C _E	0.45 ± 0.20	0.60 ± 0.19	0.46 ± 0.23	0.37 ± 0.22
	P _D	0.67 ± 0.09	0.80 ± 0.07	0.43 ± 0.19	0.06 ± 0.04
f	P _D C _E	0.73 ± 0.10	0.84 ± 0.07	0.09 ± 0.06	0.21 ± 0.11
	P _{Combo}	0.73 ± 0.13	0.84 ± 0.10	0.07 ± 0.02	0.22 ± 0.14

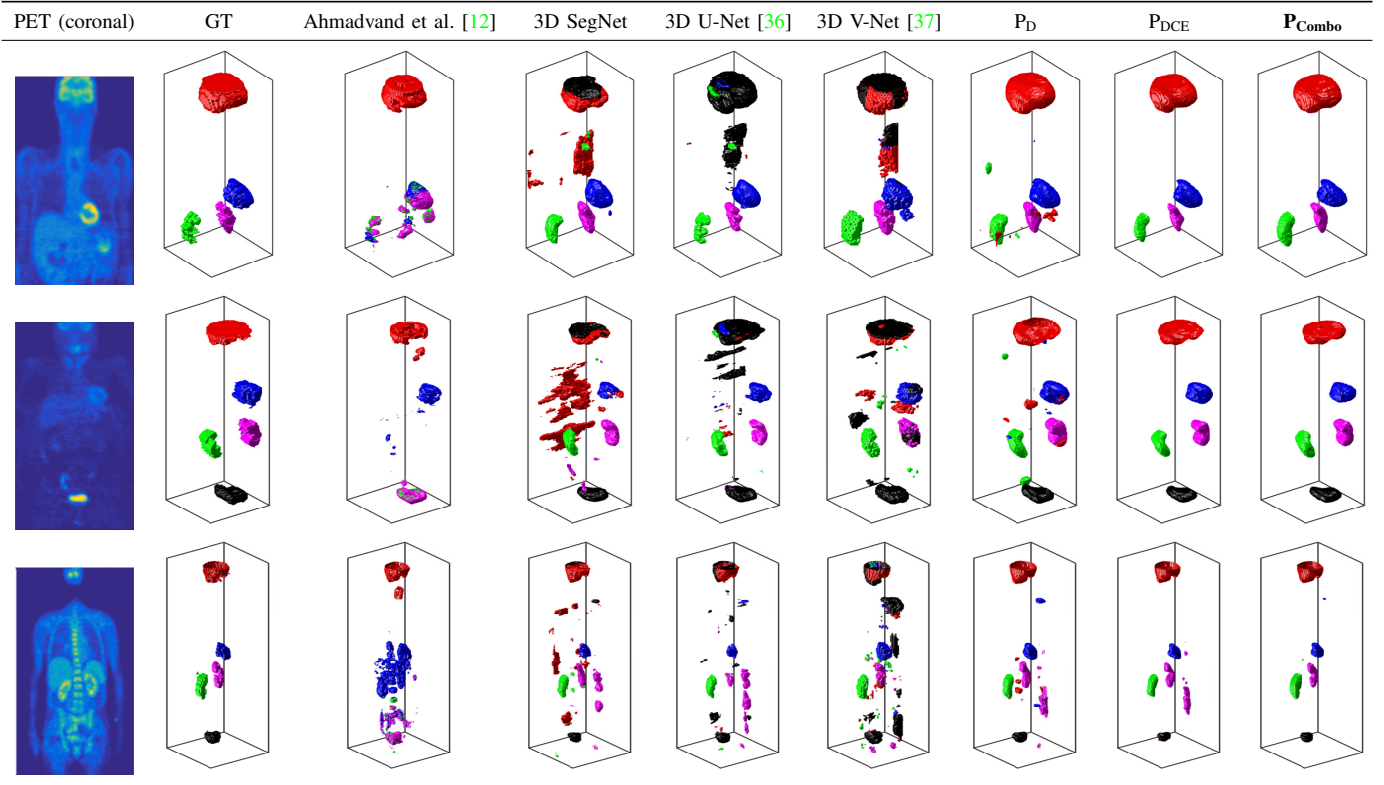


Fig. 3: Comparing multi-organ localization-segmentation-classification results of the proposed vs. competing methods. Each row shows a sample patient data.

Second, in subsection V-B, we perform similar experiments to subsection V-A for single organ segmentation from two more different modalities, i.e. MRI and ultrasound scans.

A. Performance of the proposed vs. competing methods on multi-organ PET segmentation

As reported in Table III, the proposed architecture with proposed loss (P_{Combo}) outperforms all competing methods with $57\% \pm 24\%$, $38\% \pm 18\%$, $86\% \pm 5\%$ in Jaccard, Dice and FPR, respectively. Comparing rows of section a in Table III, we note that: Modified 3D U-Net improves with our proposed loss (Combo) relatively by 23.6%, 14.5%, 56%, and 30% in Jaccard, Dice, FPR, and FNR, respectively. Comparing rows

of section b, we note that: 3D V-Net improves with our proposed loss relatively by 5.8%, 4.5%, and 28%, in Jaccard, Dice, and FPR, respectively. Section c shows that 3D SegNet improves with our proposed loss by relatively 34.1%, 23.2%, 44%, and 12.5% in Jaccard, Dice, FPR, and FNR, respectively. Comparing P_{C_E} vs. P_{WCE} in section e of Table III shows that WCE helps. Comparing P_D vs. P_{Combo} shows that the proposed Combo loss improves the results.

As shown in Figure III, although 3D U-Net, 3D V-Net, and the extended version (3D) of SegNet are able to locate the normal activities and segment them, two issues are visible: a) misclassification of organs: the competing methods were not successful in distinguishing the organs from each other, as

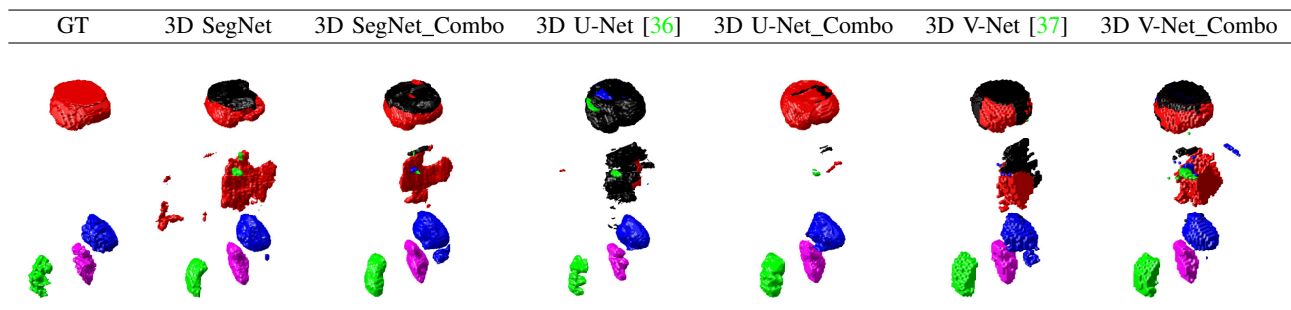


Fig. 4: Competing methods’ results before and after adding proposed loss function.

sometimes the brain (red) has been labeled as bladder (black); b) the competing methods tend to produce false positives i.e. wrongly labeling some background voxels as an organ (or one organ as another) or missing an organ (false negative). As shown in the figure, P_D still produces false positives, but no misclassification of organs. P_{CE} shows clearer segmentations, however, as we penalize the false positives more with the proposed loss we obtain much clearer outputs (last columns: P_{Combo}). The performance of the proposed method was evaluated for each specific organ and reported in Table IV.

Over all the organs, Dice scores for the proposed method (proposed architecture + Combo loss) ranges from 0.58 to 0.91. We show the worst, an in-between and the best results in terms of Dice score in Fig. 5. Although the left case in the figure seems to be the worst result in terms of Dice score, it is a difficult case with several missing organs. However, the proposed method has been able to handle multiple missing organs to a high extent. Note that some organs can be physically absent from a patient body, as in renal agenesis or radical (complete) nephrectomy, but in PET scans, there might be more “missing” organs (similar to the left case in Fig. 5) simply because of lack of radiotracer uptake in these organs thus they do not appear in PET.

TABLE IV: Organ-specific quantitative results of the proposed method for PET dataset.

	Jaccard	Dice	FPR	FNR
Brain	0.74 ± 0.20	0.83 ± 0.16	0.06 ± 0.04	0.21 ± 0.22
Heart	0.65 ± 0.15	0.78 ± 0.12	0.11 ± 0.07	0.29 ± 0.15
Left kidney	0.68 ± 0.08	0.81 ± 0.06	0.19 ± 0.15	0.20 ± 0.07
Right kidney	0.68 ± 0.10	0.81 ± 0.07	0.09 ± 0.07	0.26 ± 0.11
Bladder	0.69 ± 0.12	0.81 ± 0.09	0.04 ± 0.05	0.28 ± 0.14

Although, in training, Dice score improvement compared to 3D V-Net is small, as shown in Figure 4, in test, proposed loss helped 3D V-Net in terms of reducing organ misclassification and false positives. Looking at both Table III and Fig. 4, 3D U-Net and 3D SegNet achieved higher performance when incorporating the proposed loss.

B. Performance of the proposed vs. competing methods on single organ segmentation from MRI and ultrasound

For MRI and ultrasound datasets, we observed that all the methods are more prone to false negatives than false positives, so we weigh more the false negative term of the

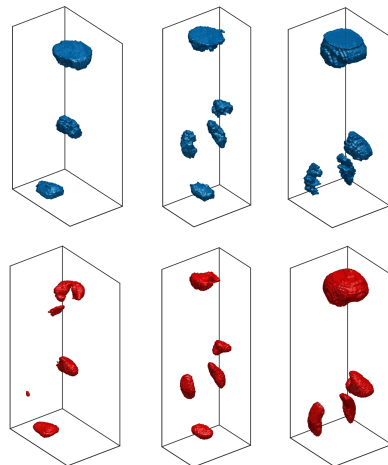


Fig. 5: Sample segmentations by the proposed method. First row shows ground truth segmentations and second row shows the proposed method results. From left to right: worst (Dice = 0.58), in-between (Dice = 0.76), and best (Dice = 0.91)

proposed loss (i.e. increase β to 0.9). As reported in Table V, similar to results in Section V-A, the Combo loss function improved 3D U-Net and 3D V-Net by 4.6% and 1.13% in Dice and 43.8% and 16.7% in FNR, respectively, for MRI prostate segmentation. Similarly, 3D U-Net and 3D V-Net results were improved by 8.23% and 3.4% in Dice and 33.3% and 16.7% in FNR, respectively, for ultrasound left ventricular myocardial segmentation.

As can also be seen in Table V, the proposed loss also helps reduce the variance of the segmentation results.

We also compared the proposed loss function with the recently introduced Focal loss function [42]. Our integrative loss function outperformed Focal loss after both were applied to different networks (Table V). We applied Focal loss to the best performing competing method for each dataset i.e. 3D V-Net for MRI and 3D U-Net for ultrasound dataset. For Focal loss, we tested several different values for α and γ , but as suggested by the authors we obtained better results with $\alpha = 0.25$ and $\gamma = 2.0$. For the MRI dataset, the proposed Combo loss outperformed Focal loss by 2.3% and 47.4% in Dice and FNR, respectively, when both were used in 3D V-Net. For the ultrasound dataset, Combo loss outperformed Focal loss by 10.8% in Dice.

TABLE V: Comparing performance of competing methods with/without proposed (_Combo) loss function vs. proposed method for MRI prostate and ultrasound left ventricular myocardial segmentation.

	Methods	Dice	FPR	FNR
MRI	3D U-Net [36]	0.87 ± 0.07	0.0004 ± 0.0004	0.16 ± 0.12
	3D U-Net_Combo	0.91 ± 0.05	0.0005 ± 0.0005	0.09 ± 0.08
	3D V-net [37]	0.88 ± 0.05	0.0006 ± 0.0004	0.12 ± 0.08
	3D V-net_Focal	0.87 ± 0.04	0.0002 ± 0.0002	0.19 ± 0.07
	3D Vnet_Combo	0.89 ± 0.05	0.0006 ± 0.0005	0.10 ± 0.08
	ProposedArc_Combo	0.90 ± 0.04	0.0007 ± 0.0006	0.08 ± 0.07
Ultrasound	3D U-Net [36]	0.85 ± 0.05	0.0020 ± 0.0006	0.12 ± 0.12
	3D U-Net_Combo	0.92 ± 0.05	0.0007 ± 0.0003	0.08 ± 0.09
	3D U-Net_Focal	0.83 ± 0.22	0.0004 ± 0.0005	0.17 ± 0.15
	3D V-net [37]	0.84 ± 0.04	0.0020 ± 0.0008	0.12 ± 0.08
	3D Vnet_Combo	0.87 ± 0.03	0.0020 ± 0.0005	0.10 ± 0.04
	ProposedArc_Combo	0.92 ± 0.05	0.0006 ± 0.0004	0.09 ± 0.10

VI. CONCLUSION

In this paper, we proposed a new loss function to handle input/class-imbalance and output imbalance (i.e. false positives and false negatives). The proposed loss function resulted in improved performance in both multi- and single-organ segmentation from different modalities. The proposed loss function also improved the existing methods in terms of achieving higher Dice and lower false positive and false negative rates. In this work, we applied the proposed loss function to a multi-organ segmentation problem, but it can simply be leveraged for other segmentation tasks as well. A potential future work would be on finding optimal values for the loss function weights using Bayesian optimization methods instead of setting them experimentally.

Disclaimer: This feature is based on research and is not commercially available. Due to regulatory reasons its future availability cannot be guaranteed.

REFERENCES

- [1] Y. Zheng, A. Barbu, B. Georgescu, M. Scheuring, and D. Comaniciu, "Four-chamber heart modeling and automatic segmentation for 3-D cardiac CT volumes using marginal space learning and steerable features," *IEEE Transactions on Medical Imaging*, vol. 27, no. 11, pp. 1668–1681, 2008.
- [2] A. Criminisi, J. Shotton, and S. Bucciarelli, "Decision forests with long-range spatial context for organ localization in CT volumes," in *Medical Image Computing and Computer-Assisted Intervention (MICCAI)*, 2009, pp. 69–80.
- [3] A. Criminisi, J. Shotton, D. Robertson, and E. Konukoglu, "Regression forests for efficient anatomy detection and localization in CT studies," in *International MICCAI Workshop on Medical Computer Vision*. Springer, 2010, pp. 106–117.
- [4] A. Criminisi, D. Robertson, E. Konukoglu, J. Shotton, S. Pathak, S. White, and K. Siddiqui, "Regression forests for efficient anatomy detection and localization in computed tomography scans," *Medical Image Analysis*, vol. 17, no. 8, pp. 1293–1303, 2013.
- [5] P. Fischer, V. Daum, D. Hahn, M. Prümmer, and J. Hornegger, "Regression forest-based organ detection in normalized PET images," in *Bildverarbeitung für die Medizin 2014*. Springer, 2014, pp. 384–389.
- [6] L. Bi, J. Kim, D. Feng, and M. Fulham, "Multi-stage thresholded region classification for whole-body PET-CT lymphoma studies," in *International Conference on Medical Image Computing and Computer-Assisted Intervention (MICCAI)*. Springer, 2014, pp. 569–576.
- [7] R. Gauriau, R. Cuingnet, D. Lesage, and I. Bloch, "Multi-organ localization with cascaded global-to-local regression and shape prior," *Medical Image Analysis*, vol. 23, no. 1, pp. 70–83, 2015.
- [8] L. Bi, J. Kim, L. Wen, D. Feng, and M. Fulham, "Automated thresholded region classification using a robust feature selection method for PET-CT," in *Biomedical Imaging (ISBI), 2015 IEEE 12th International Symposium on*. IEEE, 2015, pp. 1435–1438.
- [9] R. P. Burke, Z. Xu, C. P. Lee, R. B. Baucom, B. K. Poulouse, R. G. Abramson, and B. A. Landman, "Multi-atlas segmentation for abdominal organs with gaussian mixture models," in *Medical Imaging 2015: Biomedical Applications in Molecular, Structural, and Functional Imaging*, vol. 9417. International Society for Optics and Photonics, 2015, p. 941707.
- [10] M. Marsousi, K. N. Plataniotis, and S. Stergiopoulos, "Atlas-based segmentation of abdominal organs in 3d ultrasound, and its application in automated kidney segmentation," in *Engineering in Medicine and Biology Society (EMBC), 2015 37th Annual International Conference of the IEEE*. IEEE, 2015, pp. 2001–2005.
- [11] L. Bi, J. Kim, A. Kumar, L. Wen, D. Feng, and M. Fulham, "Automatic detection and classification of regions of FDG uptake in whole-body PET-CT lymphoma studies," *Computerized Medical Imaging and Graphics*, vol. 60, pp. 3–10, 2017.
- [12] P. Ahmadvand, N. Duggan, F. Bénard, and G. Hamarneh, "Tumor lesion segmentation from 3D PET using a machine learning driven active surface," in *International Workshop on Machine Learning in Medical Imaging*. Springer, 2016, pp. 271–278.
- [13] P. Hu, F. Wu, J. Peng, Y. Bao, F. Chen, and D. Kong, "Automatic abdominal multi-organ segmentation using deep convolutional neural network and time-implicit level sets," *International Journal of Computer Assisted Radiology and Surgery*, vol. 12, no. 3, pp. 399–411, 2017.
- [14] P. N. Samarakoon, E. Promayon, and C. Fouard, "Light random regression forests for automatic multi-organ localization in CT images," in *Biomedical Imaging (ISBI) 2017, 2017 IEEE 14th International Symposium on*. IEEE, 2017, pp. 371–374.
- [15] A. Schmidt-Richberg, T. Brosch, N. Schadewaldt, T. Klinder, A. Cavallaro, I. Salim, D. Roundhill, A. Papageorgiou, and C. Lorenz, "Abdomen segmentation in 3d fetal ultrasound using cnn-powered deformable models," in *Fetal, Infant and Ophthalmic Medical Image Analysis*. Springer, 2017, pp. 52–61.
- [16] B. D. de Vos, J. M. Wolterink, P. A. de Jong, T. Leiner, M. A. Viergever, and I. Išgum, "Convnet-based localization of anatomical structures in 3-d medical images," *IEEE Transactions on Medical Imaging*, vol. 36, no. 7, pp. 1470–1481, 2017.
- [17] D. Yang, D. Xu, S. K. Zhou, B. Georgescu, M. Chen, S. Grbic, D. Metaxas, and D. Comaniciu, "Automatic liver segmentation using an adversarial image-to-image network," in *International Conference on Medical Image Computing and Computer-Assisted Intervention*. Springer, 2017, pp. 507–515.
- [18] E. Gibson, F. Giganti, Y. Hu, E. Bonmati, S. Bandula, K. Gurusamy, B. R. Davidson, S. P. Pereira, M. J. Clarkson, and D. C. Barratt, "Towards image-guided pancreas and biliary endoscopy: Automatic multi-organ segmentation on abdominal CT with dense dilated networks," in *International Conference on Medical Image Computing and Computer-Assisted Intervention (MICCAI)*. Springer, 2017, pp. 728–736.
- [19] M. F. Bobo, S. Bao, Y. Huo, Y. Yao, J. Virostko, A. J. Plassard, I. Lyu, A. Assad, R. G. Abramson, M. A. Hilmes *et al.*, "Fully convolutional neural networks improve abdominal organ segmentation," in *Medical Imaging 2018: Image Processing*, vol. 10574. International Society for Optics and Photonics, 2018, p. 105742V.
- [20] Y. Boykov and M.-P. Jolly, "Interactive organ segmentation using graph cuts," in *International Conference on Medical Image Computing and Computer-Assisted Intervention (MICCAI)*. Springer, 2000, pp. 276–286.
- [21] S. Andrews, G. Hamarneh, and A. Saad, "Fast random walker with priors using precomputation for interactive medical image segmentation," in *International Conference on Medical Image Computing and Computer-Assisted Intervention (MICCAI)*. Springer, 2010, pp. 9–16.
- [22] A. Tsai, A. Yezzi, W. Wells, C. Tempany, D. Tucker, A. Fan, W. E. Grimson, and A. Willsky, "A shape-based approach to the segmentation of medical imagery using level sets," *IEEE Transactions on Medical Imaging*, vol. 22, no. 2, pp. 137–154, 2003.
- [23] C. McIntosh and G. Hamarneh, "Medical image segmentation: Energy minimization and deformable models."
- [24] M. S. Nosrati and G. Hamarneh, "Incorporating prior knowledge in medical image segmentation: a survey," *arXiv preprint arXiv:1607.01092*, 2016.

- [25] P. Aljabar, R. A. Heckemann, A. Hammers, J. V. Hajnal, and D. Rueckert, "Multi-atlas based segmentation of brain images: atlas selection and its effect on accuracy," *Neuroimage*, vol. 46, no. 3, pp. 726–738, 2009.
- [26] A. Sotiras, C. Davatzikos, and N. Paragios, "Deformable medical image registration: A survey," *IEEE Transactions on Medical Imaging*, vol. 32, no. 7, pp. 1153–1190, 2013.
- [27] I. Isgum, M. Staring, A. Rutten, M. Prokop, M. A. Viergever, and B. Van Ginneken, "Multi-atlas-based segmentation with local decision fusion application to cardiac and aortic segmentation in CT scans," *IEEE Transactions on Medical Imaging*, vol. 28, no. 7, pp. 1000–1010, 2009.
- [28] C. Chu, M. Oda, T. Kitahara, K. Misawa, M. Fujiwara, Y. Hayashi, Y. Nimura, D. Rueckert, and K. Mori, "Multi-organ segmentation based on spatially-divided probabilistic atlas from 3D abdominal CT images," in *International Conference on Medical Image Computing and Computer-Assisted Intervention (MICCAI)*. Springer, 2013, pp. 165–172.
- [29] Y. Yuan, M. Chao, and Y.-C. Lo, "Automatic skin lesion segmentation using deep fully convolutional networks with jaccard distance," *IEEE Transactions on Medical Imaging*, vol. 36, no. 9, pp. 1876–1886, 2017.
- [30] G. Litjens, T. Kooi, B. E. Bejnordi, A. A. A. Setio, F. Ciompi, M. Ghahfoorian, J. A. van der Laak, B. van Ginneken, and C. I. Sánchez, "A survey on deep learning in medical image analysis," *Medical Image Analysis*, vol. 42, pp. 60–88, 2017.
- [31] C. F. Baumgartner, L. M. Koch, M. Pollefeys, and E. Konukoglu, "An exploration of 2D and 3D deep learning techniques for cardiac MR image segmentation," *arXiv preprint arXiv:1709.04496*, 2017.
- [32] F. Milletari, S.-A. Ahmadi, C. Kroll, A. Plate, V. Rozanski, J. Maiostre, J. Levin, O. Dietrich, B. Ertl-Wagner, K. Bötzel *et al.*, "Hough-CNN: deep learning for segmentation of deep brain regions in mri and ultrasound," *Computer Vision and Image Understanding*, vol. 164, pp. 92–102, 2017.
- [33] G. Wang, M. A. Zuluaga, W. Li, R. Pratt, P. A. Patel, M. Aertsen, T. Doel, A. L. David, J. Deprest, S. Ourselin *et al.*, "Deepigeos: a deep interactive geodesic framework for medical image segmentation," *arXiv preprint arXiv:1707.00652*, 2017.
- [34] A. BenTaieb and G. Hamarneh, "Topology aware fully convolutional networks for histology gland segmentation," in *International Conference on Medical Image Computing and Computer-Assisted Intervention (MICCAI)*. Springer, 2016, pp. 460–468.
- [35] O. Ronneberger, P. Fischer, and T. Brox, "U-net: convolutional networks for biomedical image segmentation," in *International Conference on Medical image computing and computer-assisted intervention (MICCAI)*. Springer, 2015, pp. 234–241.
- [36] Ö. Çiçek, A. Abdulkadir, S. S. Lienkamp, T. Brox, and O. Ronneberger, "3D U-Net: learning dense volumetric segmentation from sparse annotation," in *International Conference on Medical Image Computing and Computer-Assisted Intervention (MICCAI)*. Springer, 2016, pp. 424–432.
- [37] F. Milletari, N. Navab, and S.-A. Ahmadi, "V-net: Fully convolutional neural networks for volumetric medical image segmentation," in *3D Vision (3DV), 2016 Fourth International Conference on*. IEEE, 2016, pp. 565–571.
- [38] V. Badrinarayanan, A. Kendall, and R. Cipolla, "SegNet: a deep convolutional encoder-decoder architecture for image segmentation," *IEEE Transactions on Pattern Analysis and Machine Intelligence*, vol. 39, no. 12, pp. 2481–2495, 2017.
- [39] K. H. Cha, L. Hadjiiski, R. K. Samala, H.-P. Chan, E. M. Caoili, and R. H. Cohan, "Urinary bladder segmentation in CT urography using deep-learning convolutional neural network and level sets," *Medical Physics*, vol. 43, no. 4, pp. 1882–1896, 2016.
- [40] N. V. Chawla, K. W. Bowyer, L. O. Hall, and W. P. Kegelmeyer, "Smote: synthetic minority over-sampling technique," *Journal of Artificial Intelligence Research*, vol. 16, pp. 321–357, 2002.
- [41] C. H. Sudre, W. Li, T. Vercauteren, S. Ourselin, and M. J. Cardoso, "Generalised dice overlap as a deep learning loss function for highly unbalanced segmentations," in *Deep Learning in Medical Image Analysis and Multimodal Learning for Clinical Decision Support*. Springer, 2017, pp. 240–248.
- [42] T.-Y. Lin, P. Goyal, R. Girshick, K. He, and P. Dollár, "Focal loss for dense object detection," *arXiv preprint arXiv:1708.02002*, 2017.
- [43] X. Glorot and Y. Bengio, "Understanding the difficulty of training deep feedforward neural networks," in *Proceedings of the Thirteenth International Conference on Artificial Intelligence and Statistics*, 2010, pp. 249–256.
- [44] M. D. Zeiler, "Adadelata: an adaptive learning rate method," *arXiv preprint arXiv:1212.5701*, 2012.
- [45] R. R. Beichel, E. J. Ulrich, C. Bauer, A. Wahle, B. Brown, T. Chang, K. A. Plichta, B. J. Smith, J. J. Sunderland, T. Braun, A. Fedorov, D. Clunie, M. Onken, J. Riesmeier, S. Pieper, R. Kikinis, M. M. Graham, T. L. Casavant, M. Sonka, and J. M. Buatti, "Data from QIN-HEADNECK <http://doi.org/10.7937/k9/tcia.2015.k0f5cgli>," *The Cancer Imaging Archive*, 2015.
- [46] A. Fedorov, D. Clunie, E. Ulrich, C. Bauer, A. Wahle, B. Brown, M. Onken, J. Riesmeier, S. Pieper, R. Kikinis, J. Buatti, and R. Beichel, "DICOM for quantitative imaging biomarker development: a standards based approach to sharing clinical data and structured PET/CT analysis results in head and neck cancer research. peerj 4:e2057 <https://doi.org/10.7717/peerj.2057>," 2016.
- [47] L. Geert, D. Oscar, B. Jelle, K. Nico, and H. Henkjan, "Prostatex challenge data. <https://doi.org/10.7937/k9/tcia.2017.murs5cl>," *The Cancer Imaging Archive*, 2017.
- [48] G. Litjens, O. Debats, J. Barentsz, N. Karssemeijer, and H. Huisman, "Computer-aided detection of prostate cancer in MRI," *IEEE Transactions on Medical Imaging*, vol. 33, no. 5, pp. 1083–1092, 2014.
- [49] K. Clark, B. Vendt, K. Smith, J. Freymann, J. Kirby, P. Koppel, S. Moore, S. Phillips, D. Maffitt, M. Pringle *et al.*, "The Cancer Imaging Archive (TCIA): maintaining and operating a public information repository," *Journal of Digital Imaging*, vol. 26, no. 6, pp. 1045–1057, 2013.